

Absence of Majorana oscillations in finite-length full-shell hybrid nanowires

Carlos Payá,¹ Pablo San-Jose,¹ Carlos J. Sánchez Martínez,^{2,3} Ramón Aguado,¹ and Elsa Prada^{1,*}

¹*Instituto de Ciencia de Materiales de Madrid (ICMM), CSIC, Madrid, Spain*

²*Departamento de Física Teórica de la Materia Condensada,
Universidad Autónoma de Madrid, Madrid, Spain*

³*Condensed Matter Physics Center (IFIMAC), Universidad Autónoma de Madrid, Madrid, Spain.*

(Dated: July 10, 2024)

Majorana bound states (MBSs) located at the ends of a hybrid superconductor-semiconductor nanowire are only true zero modes if their characteristic localization length is much smaller than the nanowire length, $\xi_M \ll L$. Otherwise, their wave function overlap gives rise to a finite energy splitting that shows a characteristic oscillatory pattern $\sim e^{-2L/\xi_M} \cos(k_F L)$ versus external parameters that modify the Fermi momentum k_F . Detecting such “Majorana oscillations”, measurable through low-bias conductance, has been proposed as a strategy for Majorana detection in pristine nanowires. Here we discuss how this detection scheme does not work in full-shell hybrid nanowires, an alternative design to partial-shell nanowires in which a superconductor shell fully wraps the semiconductor core. Using microscopic models, we provide both numerical simulations for Al/InAs hybrids as well as analytical approximations in terms of general nanowire parameters. We find that Majorana oscillations with flux in full-shell nanowires are absent in a wide portion of parameter space. This absence is not a signature of non-overlapping left- and right-end MBSs, but a consequence of the Majorana oscillation period being systematically larger than the flux window of odd Little-Parks lobes where Majorana zero-energy peaks are predicted to appear. Our results demonstrate that split near-zero modes or individual zero-energy crossings should not be dismissed as trivial even if they are found not to oscillate with flux.

I. INTRODUCTION

Majorana bound states (MBSs) are non-Abelian quasiparticles that appear at the ends of one-dimensional topological superconductors [1–4]. Among the various proposed platforms that host MBSs [5–8], arguably the most studied one is known as the Oreg-Lutchyn Majorana nanowire [9, 10]. It is based on hybrid superconductor-semiconductor heterostructures with strong spin-orbit coupling (SOC), which may undergo a topological transition in response to an applied Zeeman field. During the last two decades, several measurement schemes of increasing complexity have been pursued to unambiguously confirm the emergence of MBSs, including tunneling [11, 12], Coulomb [13, 14] and quantum-dot-assisted spectroscopies [15]. More recently, sophisticated protocols [16] that combine local and non-local conductance measurements using time-resolved interferometry and single-shot parity readout [17] have also been implemented. Despite such experimental efforts, interpreting the data is challenging when taking into account all the phenomenology [18] that arises in realistic hybrid systems beyond the predictions of the ideal single-mode Majorana nanowire model. Generalizations include e.g. the effects of disorder and material inhomogeneities [19, 20].

In pristine Oreg-Lutchyn nanowires, a way to identify MBSs was proposed already in 2012 [21], see also Refs. 22 and 23. In a finite-length nanowire whose length L is not much larger than the Majorana localization length,

ξ_M , the left- and right-end MBS wave functions spatially overlap, see Fig. 1. This gives rise to a splitting $\sim e^{-2L/\xi_M} \cos(k_F L)$ of the zero-energy Majorana mode that decays exponentially with L , just as the overlap, but that also has a sinusoidal behavior with Fermi momentum k_F . This in turn could be detected as a characteristic oscillatory splitting with Zeeman field (or chemical potential) of the zero-bias conductance peak in tunneling spectroscopy measurements.

While Majorana oscillations have been studied in different contexts in Zeeman-driven nanowires [24, 25], including critical current oscillations in Josephson junctions [26], they have not yet been analyzed in a full-shell hybrid geometry. Full-shell hybrid nanowires are an alternative Majorana nanowire design that came to the spotlight in 2020 [13] in which the superconductor shell that induces superconductivity into the semiconductor core is not limited to some facets of the nanowire, but wraps it all around. The doubly-connected geometry of the superconductor has profound implications in the response of these wires to an applied axial magnetic field. It gives rise for instance to the Little-Parks (LP) effect [27, 28], whereby the superconducting order parameter oscillates with flux in a series of *lobes* characterized by an integer number n of superconductor phase windings, called fluxoids. It also enables the presence of a special type of subgap Andreev states [29–33] that have been called Caroli-de Gennes-Matricon (CdGM) analog states [34]. In the topological phase, one of those subgap states transforms into a Majorana zero mode, extending across a flux interval inside odd- n LP lobes [13, 35, 36]. Importantly, the topological superconducting properties are not driven by the Zeeman effect, but by the orbital

* elsa.prada@csic.es

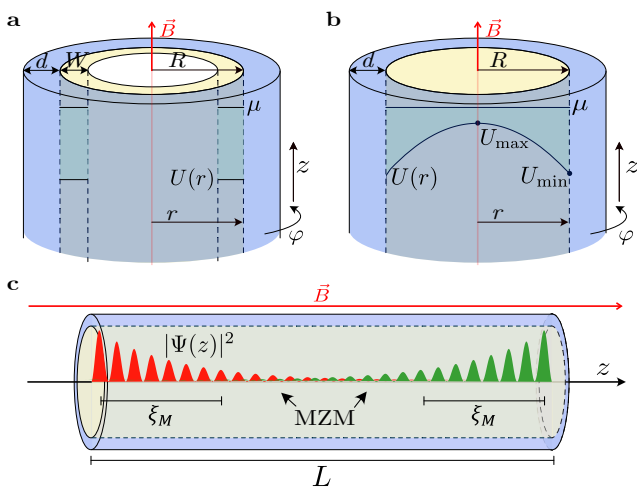


FIG. 1. **Full-shell hybrid nanowire.** (a) Sketch of a full-shell nanowire with a tubular-core geometry. An insulating core (white) is surrounded by a semiconductor tube (yellow) of external radius R and thickness W , and is completely encapsulated in a thin superconductor shell (blue) of thickness d . In an applied axial magnetic field B the hybrid wire is threaded by a non-quantized magnetic flux $\Phi = \pi(R+d/2)^2 B$. The chemical potential μ and the radial electrostatic potential $U(r)$ are schematically depicted inside. (b) Same as (a) but for a semiconductor solid-core geometry. The conduction-band bottom inside the semiconductor exhibits a dome-like radial profile with maximum value at the center, U_{\max} , and minimum value at the superconductor-semiconductor interface, U_{\min} . (c) Sketch of a full-shell nanowire of finite length L in the topological phase. In red and green, Majorana bound state (MBS) wavefunctions at the left and right ends of the nanowire along the longitudinal direction. ξ_M is the Majorana localization length.

effect of the magnetic field, which among other things permits operating these wires at much smaller magnetic field than their partial-shell counterparts. The rich phenomenology of these wires is being analyzed in recent years [14, 36–46], but there are still many basic questions that need to be understood.

In this work we consider the effect of finite nanowire length on the Majorana zero modes. We find that the expected Majorana oscillations are absent for a wide (and realistic) region of parameter space. This hinders the possibility of using Majorana oscillations as a way to identify and characterize MBSs in full-shell wires. We consider both microscopic numerical simulations in perfect Al/InAs full-shell nanowires as well as general analytical derivations as a function of the hybrid parameters. The absence of oscillations is not a consequence of the left and right-end MBSs not overlapping in a finite- L nanowire. Actually, zero energy modes in full-shell geometries still split as $\sim e^{-2L/\xi_M} \cos(k_F L)$ when the nanowire length L is not much larger than the Majorana localization length ξ_M . The reason is that, except for very narrow and long wires, the Ma-

jorana oscillation period with flux, which we show to be $\delta\Phi = 2\pi/|L\partial_\Phi k_F(\Phi)|$, is systematically of the order or larger than the lobe flux window. The practical consequence is that a lack of oscillations around zero of a near-zero mode or parity crossing cannot be used to rule out a topological origin.

This paper is organized as follows. In Sec. II we explain the two different realistic models that we consider for the full-shell hybrid geometry: the tubular-core nanowire, analyzed in Sec. II A, and the solid core nanowire, analyzed in Sec. II B. In Sec. III we provide a discussion of the results. A summary of our findings and the conclusions of this work are given in Sec. IV. In Appendix A we provide the Hamiltonians employed to analyze these hybrid wires, including the tubular-core approximation and the mapping to the Oreg-Lutchyn model (Appendix A 1). An analytical expression for the Majorana oscillation period in full-shell hybrid nanowires is derived in Appendix B, together with an analysis of the typical range of parameters for which there are no Majorana oscillations. While the numerical results we present in the main text correspond to a wire in the non-destructive LP regime, the destructive one is considered in Appendix C.

II. MODELS AND RESULTS

A full-shell hybrid nanowire with a semiconductor core of radius R and a thin superconductor shell of thickness d is shown in Fig. 1. We consider two possible realistic models for the semiconductor core [36]. In the first one, Fig. 1(a), the interior is insulating around the axis and the semiconductor has a tubular shape of thickness W . This is called the tubular-core model. In the second one, Fig. 1(b), the semiconductor completely fills the interior of the shell. This is dubbed the solid-core model.

In our models we employ cylindrical coordinates, with radial coordinate denoted by r , azimuthal angle by φ and axial coordinate chosen along the z direction. For simplicity, we assume that the hybrid wire has cylindrical symmetry. It has been shown that this is a very good approximation for a more realistic hexagonal-shaped nanowire [34, 36]. The full-shell nanowire is threaded by a magnetic field $\vec{B} = B\hat{z}$ that gives rise to a flux $\Phi = \pi R_{\text{LP}}^2 B$, where we define the LP radius as $R_{\text{LP}} = R + d/2$, the mean radius of the shell.

The methodology to analyze these wires, both analytically and numerically, has been thoroughly described in Refs. [13, 34, 36]. We provide a summary in Appendix A. As discussed there, it is possible to arrive at an effective Bogoliubov-de Gennes (BdG) Hamiltonian for the hybrid system, see Eq. (A3). The Hamiltonian is expressed in terms of the flux Φ , which, in units of the superconducting flux quantum $\Phi_0 = h/2e$ (where h is the Planck constant and e the electron charge), defines the fluxoid $n(\Phi) = \lfloor \Phi/\Phi_0 \rfloor$. This is the number of times the superconductor phase winds around the wire axis for

a given flux. Other variables include nanowire intrinsic parameters such as the effective mass m , the chemical potential μ , the SOC α and the g -factor, the geometrical parameters (d , R , W), the radial electrostatic potential energy $U(r)$, the decay rate from the semiconductor core into the superconductor Γ_S , the shell superconducting gap at zero field Δ_0 , the diffusive superconducting coherence length ξ_d , and the radial and generalized angular momentum quantum numbers (m_r, m_J) that label the different transverse subbands of the wire.

Previous results in Ref. [36] analyzed in detail the phenomenology of a semi-infinite full-shell nanowire, including the topological phase diagrams as a function of R , W , α , μ and Γ_S , the local density of states (LDOS) at the end of the wire, and the differential conductance through a normal-superconductor junction. In this work we consider the phenomenology of these wires when they have a finite length L so that, in the topological regime, left- and right-end MBSs can overlap, see Fig. 1(c).

In our numerical simulations of the main text and the Appendix C we will employ typical parameters for an Al/InAs hybrid nanowire, since those are the most common materials analyzed experimentally so far. We note that, recently, a practical theoretical proposal based on semiconductor hole bands (instead of electron bands as here) was studied in Ref. [47] for InP/GaSb core-shell nanowires. General analytical results for the Majorana splittings can be found in Appendix B.

A. Tubular-core nanowire

We start by analyzing a full-shell hybrid nanowire with a tubular core, see Fig. 1(a). This model could describe a multi-shell nanowire with an insulating core and a semiconductor shell (a so-called core-shell nanowire in the literature), fully wrapped in a superconductor shell.

In Fig. 2(a) we can see the LDOS of a semi-infinite tubular-core nanowire. It is represented against the flux Φ through the LP section normalized to Φ_0 . This flux causes the superconducting phase in the shell to acquire a quantized winding $n = 0, \pm 1, \pm 2, \dots$ around the nanowire axis. Winding number jumps are accompanied by a repeated suppression and recovery of the superconductor shell gap, forming so-called LP lobes as a function of flux, characterized by the integer number n of fluxoids through the section. In Fig. 2(a) we show half of the $n = 0$ and the full $n = 1 - 3$ lobes. We observe a number of bright features below the parent gap in the different lobes. These are the so-called CdGM analog states analyzed in detail Ref. [34, 36]. They are Van Hove singularities that are induced by the superconductor shell on the normal core bands. The geometrical parameters (core radius $R = 70$ nm and shell thickness $d = 10$ nm) and the superconductor parameters (gap at zero field $\Delta_0 = 0.23$ meV and diffusive superconducting coherence length $\xi_d = 70$ nm) are such that the wire is in the non-destructive LP regime, meaning that the parent

gap does not close between lobes at half integer values of Φ_0 . As a result, all the subgap features change abruptly at fluxoids jumps between lobes. The transition from the non-destructive to the destructive LP regime [48], analyzed in Appendix C, typically happens for smaller R_{LP} radius, see Eq. (A13).

In a full-shell nanowire that can be described with a cylindrical approximation, MBSs are predicted to appear at odd LP lobes when the parameters of the wire are such that the system is the topological phase, see Appendix A. When the thickness of the tubular semiconductor, W , is small compared to its radius R , it is possible to approximate the radial electrostatic energy $U(r)$ and the SOC $\alpha(r)$ as constants, see Fig. 1(a). When the doping of the semiconductor wire is small, as it is typically the case in depleted nanowires, only the lowest radial subband is populated and the Hamiltonian of the system can be approximated by Eq. (A14), given in terms of the average radius R_{av} of electron wave functions inside the semiconductor. In this case, for the subband with lowest generalized angular momentum $m_J = 0$ there is a direct mapping to the single-mode Oreg-Lutchyn model, see Ref. [13] and Appendix A 1. It is then straightforward to understand the appearance of Majorana zero energy modes in odd lobes, since these are the only ones where m_J can take a zero value. This mapping is also very useful to appreciate that the topological phase transition in full-shell nanowires is driven by an orbital effect, see the expression for the *effective* Zeeman field, Eq. (A17).

Since in Fig. 2(a) the values of α , μ and Γ_S have been chosen so that the full-shell wire is in the topological regime, we can observe a zero-energy peak (ZEP) in the $n = 1$ lobe that emerges due to the presence of a MBS at the end of the semi-infinite wire at zero energy. It extends from the left end of the lobe to an intermediate value of flux within the lobe, as corresponds to a tubular-core nanowire. At the right end of the ZEP, the topological band closing and reopening of the $m_J = 0$ subband is visible. At the left end a CdGM state crosses zero energy. Still, there is a region of fluxes where the Majorana mode is spectrally separated from other subgap states and is thus protected by a topological minigap. For the parameters of this wire, there is also a ZEP in the $n = 3$ lobe that crosses the whole lobe. However, it coexists with a finite LDOS background from the rest of the occupied CdGM analogs, so it is unprotected.

For illustrative purposes, in Figs. 2(b) and (c) we show the $m_J = 0$ contribution to the LDOS as a function of flux by artificially fixing the fluxoid number to $n = 1$ and $n = 3$, respectively. We moreover remove the LP modulation [by taking $\xi_d = 0$ in Eq. (A12)] to observe more clearly the subgap phenomenology. Only the magnetic flux region bounded within vertical dashed lines (the actual lobe) corresponds to a stable real solution, but we display a much larger flux range to observe the whole interval of the Majorana zero-energy anomaly, from its appearance (sometimes within the actual lobe) to its disappearance (typically at large negative flux). One could

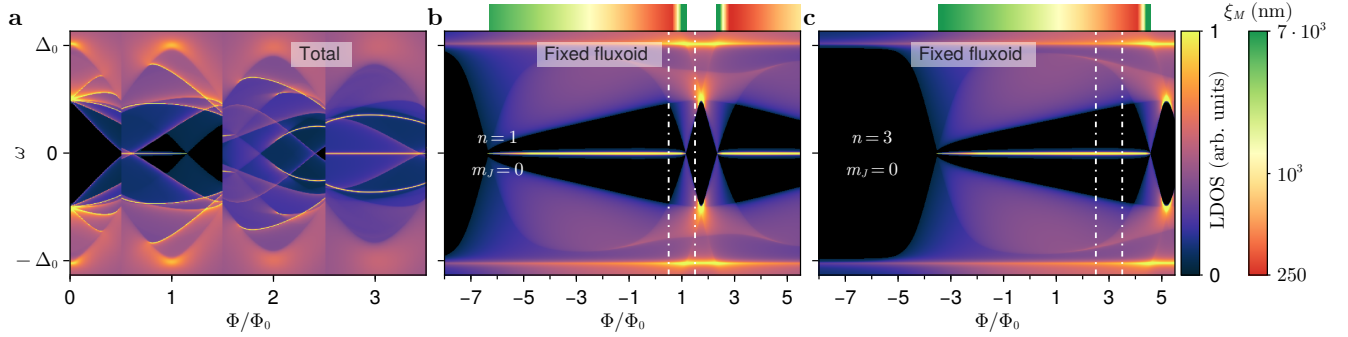


FIG. 2. **Tubular-core nanowire of semi-infinite length.** (a) Local density of states (LDOS) at the end of a semi-infinite $d = 10$ nm, $R = 70$ nm, and $W = 20$ nm tubular-core nanowire (in arbitrary units) as a function of energy ω and applied normalized magnetic flux Φ/Φ_0 , displaying half of the $n = 0$, and the full $n = 1, 2, 3$ Little-Parks (LP) lobes. Majorana zero modes are visible in the $n = 1$ and $n = 3$ LP lobes. The full-shell wire is in the non-destructive LP regime. Other subgap features are Caroli-de Gennes-Matricon (CdGM) analog states. (b) Contribution of the subbands with $m_J = 0$ generalized-angular-momentum quantum number to the LDOS in (a) but suppressing the LP modulation and fixing the fluxoid number to $n = 1$ for all the flux range displayed. The boundaries of the first LP lobe are marked with vertical dashed lines. The Majorana localization length ξ_M (in nm) as a function of flux is shown above with a color bar. (c) Same as (b) but for the $n = 3$ fluxoid number. Minimum ξ_M inside lobe $n = 1$: ~ 260 nm, inside lobe $n = 3$: ~ 290 nm. Other parameters: $\alpha = 50$ meVnm, $\mu = 18.1$ meV, $g = 10$, $\Gamma_S = 10\Delta_0$, $\Delta_0 = 0.23$ meV, $\xi_d = 70$ nm.

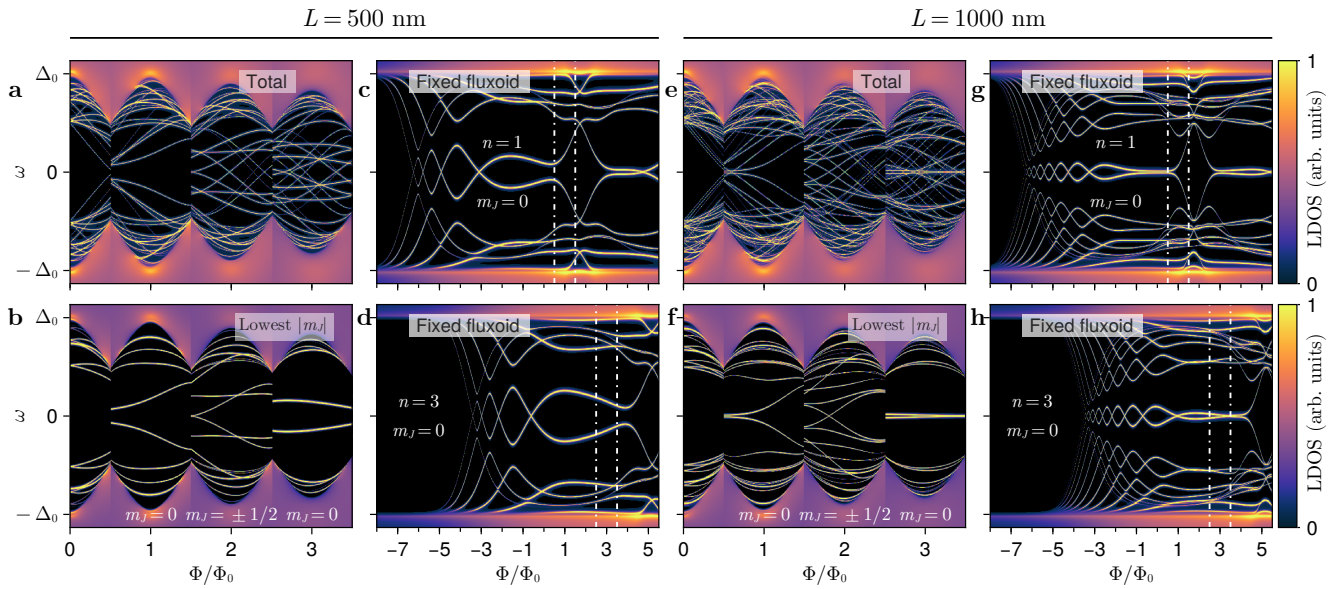


FIG. 3. **Tubular-core nanowire of finite length.** (a) Local density of states (LDOS) at the end of a $L = 500$ nm, $d = 10$ nm, $R = 70$ nm, and $W = 20$ nm tubular-core nanowire (in arbitrary units) as a function of energy ω and applied normalized flux Φ/Φ_0 , displaying half of the $n = 0$, and the full $n = 1, 2, 3$ LP lobes. (b) Contribution of the lowest m_J quantum numbers to the LDOS in (a) ($m_J = 0$ for odd lobes, $m_J = \pm 1/2$ for even lobes). (c) $m_J = 0$ contribution to the LDOS in (a) but suppressing the LP modulation and fixing the fluxoid number to $n = 1$ for all the magnetic-flux range displayed. The boundaries of the first LP lobe are marked with vertical dashed lines. (d) Same as (c) but for the $n = 3$ fluxoid number. (e-h) Same as (a-d) but for a $L = 1000$ nm full-shell nanowire. Other parameters like in Fig. 2.

think of this plot as a metastable solution of the full-shell wire if it were possible to quickly vary the magnetic flux so that the the system does not reach its ground state, thus leading to a fixed fluxoid. While this is probably possible for some flux range close to the actual lobe, it

is clearly impossible for the magnetic range shown. Still, this kind of plots provide a useful view into the behavior of the Majorana oscillations with flux in a finite-length wire and their absence within the flux windows of odd lobes.

In Fig. 2(b) the ZEP within the $n = 1$ lobe is dominated by the $k_z = 0$ gap of the $m_J = 0$ subband (the so-called inner gap that undergoes the topological inversion), whereas the one at $k_z = k_F$ (the outer gap) takes over for flux values outside the lobe. The Majorana localization length ξ_M is an important quantity to later understand Majorana overlap in the finite length case. In Fig. 2 we compute ξ_M numerically [36] and display it above the LDOS plots with a color bar (again, only the part within the vertical dashed lines is physically meaningful). In this case, ξ_M reaches a minimum of $\xi_M \approx 260$ nm precisely at the left end of the $n = 1$ lobe. ξ_M is larger in the third lobe (with a minimum of ≈ 290 nm) as the ZEP is dominated there by a smaller $m_J = 0$ minigap, namely the outer gap, which monotonically decreases until it closes for negative Φ/Φ_0 . The behaviour described above is typical for tubular-core models.

If now we consider the same parameters as in Fig. 2 but for a finite-length nanowire, we arrive at the behavior observed in Fig. 3. The total LDOS for $L = 500$ nm can be seen in Fig. 2(a). This length is approximately twice the Majorana localization length within the first lobe, so that the left and right Majoranas overlap considerably. Two striking differences appear with respect to the semi-infinite case. On the one hand, the smooth Van Hove signals that characterized the CdGM analogs in Fig. 2(a) are now transformed into a series of discrete levels for each m_J . These levels are longitudinally confined CdGM states. On the other hand, the Majorana ZEP splits into two trivial states, with a splitting that grows as the length is reduced. To see this more clearly, in Fig. 3(b) we plot the contribution to the LDOS of only the lowest $|m_J|$ subbands for each lobe, i.e. $m_J = 0$ ($m_J = \pm 1/2$) for odd (even) lobes. Notice that the third lobe ZEP is also split. The fixed-fluxoid $m_J = 0$ LDOS plots for $n = 1$ and $n = 3$ are shown in Figs. 3(c,d), respectively. It is possible to see that for large negative fluxes the ZEP does indeed oscillate with magnetic field, but this happens far away from the measurable region within the lobe boundaries (vertical dashed white lines).

Corresponding results for an $L = 1000$ nm wire are shown in Figs. 3(e-h). Since the wire is longer, the Majorana oscillations in Figs. 3(g,h) have smaller amplitude and shorter period, so that there is a larger number of oscillations along the full flux range of the zero-energy anomaly. Still, within the $n = 1$ and $n = 3$ lobes we just observe a split Majorana state, but not a full oscillation. The reason is twofold. First, at least in the $n = 1$ lobe, we are accessing only the beginning of the Majorana zero mode after the topological phase transition, where the ZEP has not yet started to oscillate significantly because it is dominated by the $k_z = 0$ gap, see Figs. 3(c,g). Second, and more importantly, the oscillation period of the Majorana is larger than the flux range it occupies within the lobe. This can be seen for instance in Fig. 3(h). One may ask whether the absence of Majorana oscillations is a peculiarity specific to tubular-core models but not to solid-core ones. The answer is negative. We analyze this

in the next section.

B. Solid-core nanowire

An equivalent study to Fig. 2 but for a semi-infinite solid-core model is shown in Fig. 4. As before, $R = 70$ nm and $d = 10$ nm, but now we have a dome-like electrostatic potential profile within the semiconductor [49, 50], see Fig. 1(b). The chosen parameters correspond to nanowire in the topological regime. Consequently, a Majorana ZEP extends throughout the first lobe corresponding to the second ($m_r = 1$) radial momentum subband. There are no Majoranas in the third lobe. In the $n = 1$ lobe there is no topological minigap since many CdGM analogs cross zero energy at different fluxes. As thoroughly analyzed in Ref. [36], this is a general trait of solid-core nanowires and is an indirect result of the radial profile of the wave function in this model, which may extend closer to the nanowire axis as compared to the tubular-core case. Only in the presence of mode mixing perturbations is it possible to open minigaps (as well as create MBSs in the $n = 0, 2$ lobes). We ignore this possibility for simplicity, as it does not affect the conclusions about Majorana oscillations studied here.

In Fig. 4(b) we observe the whole Majorana ZEP interval for a fixed $n = 1$ fluxoid as before. Note that the $m_r = 1$ ZEP that spans the vertical dashed white lines disappears for a magnetic flux of $\Phi/\Phi_0 \approx -12$. Subsequently, another ZEP emerges for more negative flux values. This second anomaly corresponds to the $m_r = 0$ topological subband. In the $n = 3$ fixed-fluxoid case of Fig. 4(c), there is no ZEP in the third lobe because only at very negative fluxes a $m_r = 0$ Majorana ZEP appears. The Majorana localization length is represented above these plots as before, and is systematically dominated by the outer gap. The minimum ξ_M within the first lobe is now more than 3 times larger than in the tubular-core case of Fig. 2.

The finite-length version of solid-core nanowire is analyzed in Fig. 5. Now we consider $L = 500$ nm in Fig. 5(a-d) and $L = 2000$ nm in Fig. 5(g-h). Once more, even if Majorana oscillations are visible in the artificial fixed-fluxoid panels, these oscillations have always a larger flux period than the flux window of the first lobe. Thus, in practice, Majorana splittings are observed in the LDOS of Figs. 5(b,f), as corresponds to overlapping left and right Majorana wave functions, but full oscillations have no flux range to develop. On the other hand, the total LDOS of Figs. 5(a,e) is covered around zero energy by many longitudinally confined CdGM analog states, the more the larger L , which hinders the observation of the Majorana peaks.

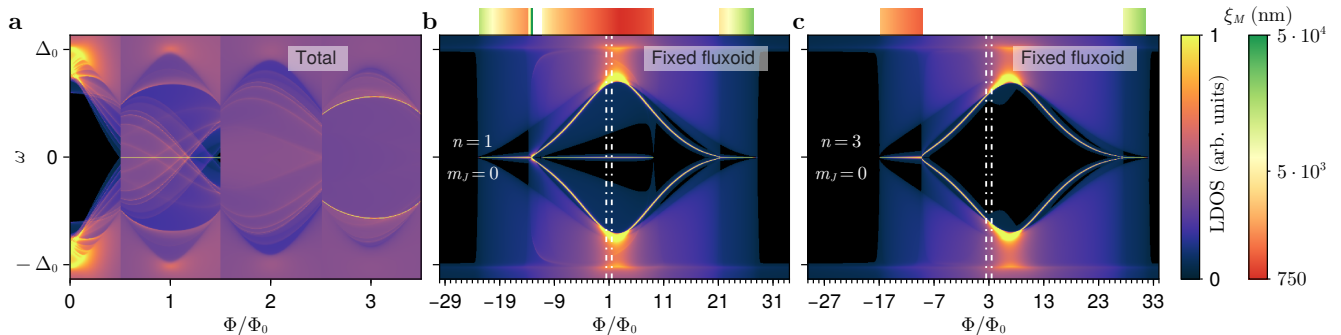


FIG. 4. **Solid-core nanowire of semi-infinite length.** Same as Fig. 2 but for a solid-core nanowire with $d = 10$ nm and $R = 70$ nm. The radial dome-like electrostatic potential profile inside the semiconductor has $U_{\min} = -30$ meV and $U_{\max} = 0$, with $\mu = 2$ meV. Other parameters like in Fig. 2, except for $\langle\alpha\rangle = 20$ meVnm and $\Gamma_S = 40\Delta_0$. Minimum ξ_M inside lobe $n = 1$: ~ 890 nm.

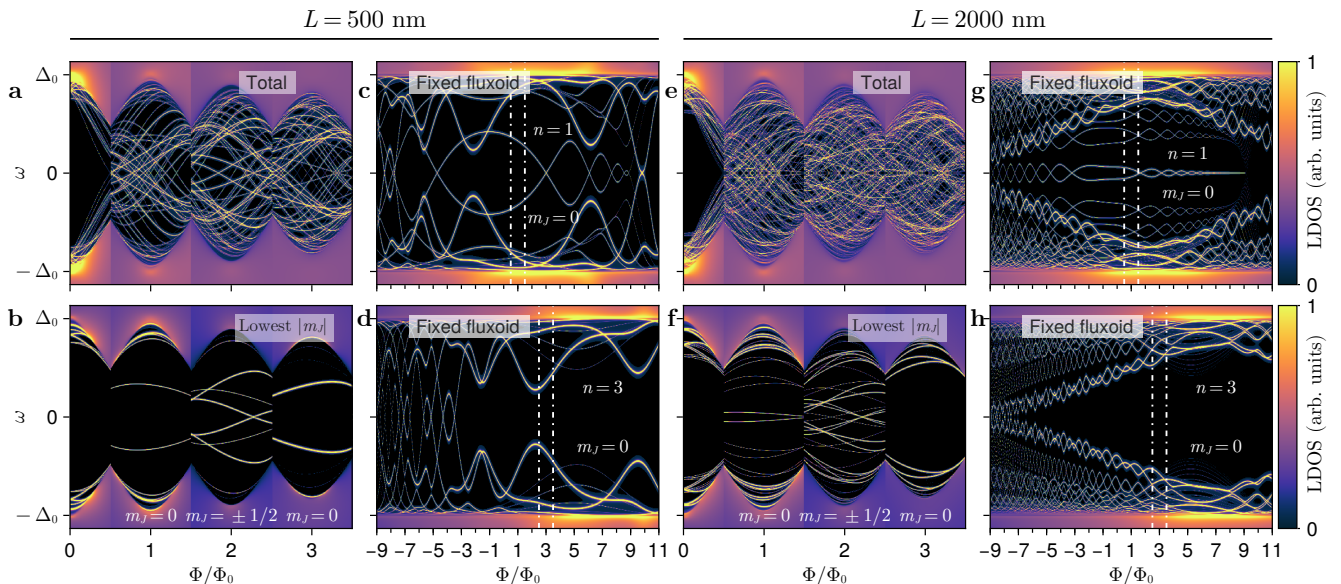


FIG. 5. **Solid-core nanowire of finite length.** Same as Fig. 3 but for a solid-core nanowire with $d = 10$ nm and $R = 70$ nm, and nanowire length $L = 500$ nm in (a-d) and $L = 2000$ nm in (e-h). Other parameters like in Fig. 4.

III. DISCUSSION

It is possible to understand the absence of Majorana oscillations observed in the previous section analytically for the tubular-core model thanks to the mapping between the single-mode Oreg-Lutchyn Hamiltonian and the $m_J = 0$ full-shell nanowire Hamiltonian. In Appendix B we derive the Majorana oscillation period $\delta\Phi$, Eq. (B5), as a function of flux and the rest of the hybrid nanowire parameters. We then compare it with the flux interval that contains Majoranas for a particular lobe n in the topological phase, I_Φ^n , which we can also derive analytically. By inserting numbers for Al/InAs, it is possible to see that $\delta\Phi \gtrsim I_\Phi^n$ and thus Majorana oscillation cannot fully develop in lobes $n = 1$ and $n = 3$ for the typical

range of parameters: $m = 0.023m_e$, $\xi_d \in [40, 250]$ nm, $L < 1.5 \mu\text{m}$, $R_{LP} \geq R_{av} > 40$ nm, $\alpha > 5$ meVnm and $\Delta > 0.05$ meV. A marginal exception to this rule are long ($L > 2\mu\text{m}$) and narrow ($R_{LP} < 40$ nm) nanowires, which may develop around one oscillation within odd lobes. Obviously, very long wires have the problem that they are more prone to have disorder along the wire and thus Majoranas can be easily destroyed. Even if disorder is sufficiently weak, the amplitude of Majorana oscillations would be exponentially suppressed with length, so that in practice the oscillations would be unobservable. On the other hand, in very narrow nanowires, even though the Majorana oscillation period decreases (with respect to wider ones), the lobe flux window also decreases, again hindering the development of proper Majorana oscillations.

tions.

We analyze this narrow regime in Appendix C. There, we consider a hybrid nanowire with $d = 10$ nm and $R = 30$ nm, both in the tubular-core (Figs. 6 and 7) and the solid-core regimes (Figs. 8 and 9). Keeping ξ_d the same, the full-shell hybrid enters the LP destructive regime when R_{LP} decreases sufficiently [48], see Eq. (A13). Two important differences with respect to the non-destructive regime are: (a) there are gapless regions between lobes and thus the flux window of each lobe decreases as n increases; and (b) the minimum SOC value to enter the topological phase in the tubular-core model strongly decreases with smaller R [36]. Apart from these differences, the conclusions with respect to the absence of Majorana oscillations are similar to the ones in Sec. II. As long as the hybrid nanowire parameters are within the ranges mentioned above, the oscillation period with flux $\delta\Phi$ is of the order or larger than the Majorana flux interval I_{Φ}^n , or even the full lobe width.

IV. CONCLUSIONS

In this work we have analyzed full-shell hybrid nanowires of finite length in the topological regime. On the one hand, subgap CdGM analog states, which in semi-infinite nanowires are Van Hove singularities induced by the superconductor shell on the semiconductor m_J propagating subbands, get longitudinally confined by the finite L and give rise to a dense collection of subgap levels that disperse with flux and that can cross zero energy. On the other hand, Majorana ZEPs that appear for a certain flux interval in the $m_J = 0$ sector within odd lobes, split in energy due to the overlap between the left and right MBSs forming at the ends of the finite- L wire.

We have focused on the fate of the Majorana splittings versus magnetic flux. In microscopic numerical simulations performed for Al/InAs hybrids, we have found that while split Majorana ZEPs appear for a wide range of parameters, there is typically no room for proper oscillations within the flux window of actual odd LP lobes. At most, a single parity crossing may occur inside the lobe. This has been confirmed analytically in Appendix B, where we show that in full-shell tubular-core nanowires $\delta\Phi \gtrsim I_{\Phi}^n$, where $\delta\Phi$ is the Majorana oscillation period and I_{Φ}^n is the flux interval that contains Majoranas for a particular lobe n . Our prediction is compatible with measurements of the lowest energy mode in full-shell islands using Coulomb spectroscopy [13], where finite length-dependent splittings in the first lobe were resolved, but not oscillations.

While our focus in the main text has been the non-destructive LP regime, the corresponding study for a hybrid nanowire in the destructive LP regime can be found in Appendix C. The conclusions are similar in this case. In principle, the Majorana oscillation period $\delta\Phi$ decreases for narrower wires, but so does the lobe width due to

the gapless regions that appear between lobes in the destructive LP regime. As a consequence, the flux window available for Majorana oscillations decreases, once more hindering their observation.

We have restricted our study to full-shell nanowires free from all types of disorder or imperfections, since our motivation is to establish the ideal baseline for the observation of Majorana oscillations. Mode-mixing disorder (i.e., disorder in the transversal direction only) was analysed before [13, 35, 36]. This type of disorder can actually be beneficial for the protection of MBSs, since it can open minigaps around zero energy by coupling different CdGM analog states. Otherwise, this type of disorder would not affect the conclusions about Majorana oscillations analyzed here. Strong disorder along the nanowire axis is however more detrimental [51–53]. As in conventional Zeeman-driven partial-shell nanowires, we expect this type of disorder to destroy MBSs and/or create quasi-Majoranas [19, 54–58], which would complicate the interpretation of the subgap phenomenology with local probes [18].

Studies of Majorana oscillations, as the one performed in this work, are important because these oscillations are often a target in experiments, since they were predicted to be a characteristic signature of topological Majorana modes [21]. Our results suggest that oscillations versus flux are however not the signature to search for in tunneling spectroscopy experiments on full-shell nanowires when trying to identify potential Majorana peaks. A given, non-oscillating, near-zero peak (or a parity crossing) in a sufficiently short full-shell wire could be interpreted as a mere longitudinally-quantized CdGM analog or a quantum-dot-like state, both topologically trivial. However, the wire could in fact be in the topological phase, and the non-oscillating peak could correspond to a pair of split Majoranas that would be stabilized to zero energy by increasing the length of the device or reducing its disorder. These considerations should also be relevant beyond tunneling spectroscopy experiments, e.g., in Josephson effect devices [59].

All the numerical code used in this manuscript was based on the Quantica.jl package [60]. The specific code to build the nanowire Hamiltonian and to perform and plot the calculations is available at Ref. [61] and Ref. [62] respectively. Visualizations were made with the Makie.jl package [63].

ACKNOWLEDGMENTS

This research was supported by Grants PID2021-122769NB-I00, PID2021-125343NB-I00 and PRE2022-101362 funded by MICIU/AEI/10.13039/501100011033, “ERDF A way of making Europe” and “ESF+”.

Appendix A: Hamiltonian

A detailed explanation of our models and methodology for studying full-shell hybrid nanowire can be found in Appendix A of Ref. [36]. There, the reader can find a discussion of the LP effect of the shell, the Bogoliubov-de Gennes (BdG) Hamiltonian, the quantum numbers for a cylindrical full-shell nanowire, the numerical methods for the Green's functions, and the expressions for the LDOS, differential conductance dI/dV and Majorana localization length ξ_M . Here, we just provide a summary of the main concepts and the Hamiltonian employed in our calculations to establish the definitions of all parameters. We refer the reader to Ref. [36] for further details.

The full-shell nanowire is a hybrid structure consisting of a superconductor shell and a semiconductor core. In the Nambu basis $\Psi = (\psi_\uparrow, \psi_\downarrow, \psi_\downarrow^\dagger, -\psi_\uparrow^\dagger)$, the BdG Hamiltonian is given by

$$H_{\text{BdG}} = \begin{bmatrix} H_0 & \Delta^\dagger \\ \Delta & -\sigma_y H_0^T \sigma_y \end{bmatrix}. \quad (\text{A1})$$

Here, H_0 is the Hamiltonian of the hybrid system in the normal state and Δ is the superconducting order parameter, that is only non-zero inside the shell. In the presence of a magnetic field $\vec{B} = B\hat{z}$ applied along the wire's axis, the vector potential in the symmetric gauge reads $\vec{A} = \frac{1}{2}(\vec{B} \times \vec{r}) = (-y, x, 0)B_z/2 = A_\varphi\hat{\varphi}$, where $A_\varphi = Br/2$. Here r is the radial coordinate and φ denotes the azimuthal angle around \hat{z} , as we want to work in cylindrical coordinates. The magnetic field threads a flux through the cylinder, defined as $\Phi = \pi R_{\text{LP}}^2 B_z$, with $R_{\text{LP}} = R + d/2$, where R is the semiconductor radius and d is the superconductor thickness. The flux Φ is thus defined at the mean radius R_{LP} of the shell. σ_i , with $i = (x, y, z)$, are Pauli matrices in the spin sector. We take $\hbar = 1$ for simplicity.

The normal Hamiltonian H_0 in Eq. (A1) is composed of H_{core} and the shell Hamiltonian in the normal state. In the normal state, the shell is a dense diffusive metal, with much smaller Fermi wavelength than the semiconductor. It is in general quite demanding to include the superconducting shell explicitly in the numerical solution of the Hamiltonian. We then choose to write an *effective* BdG Hamiltonian H of the proximitized nanowire by integrating out the shell degrees of freedom. This procedure introduces a self energy Σ_{shell} into the Green's function $G(\omega) = [\omega - H_{\text{core}} - \Sigma_{\text{shell}}(\omega)]^{-1}$. This Σ_{shell} acts on the core surface $r = R$. We thus define the effective BdG Hamiltonian for the system as $H \equiv \omega - G^{-1}(\omega) = H_{\text{core}} + \Sigma_{\text{shell}}(\omega)$, which is in general frequency dependent.

It is possible to define a generalized angular momentum as $J_z = -i\partial_\varphi + \frac{1}{2}\sigma_z + \frac{1}{2}n\tau_z$, which is the sum of the orbital angular momentum $l_z = -i\partial_\varphi$, the spin momentum $s_z = \frac{1}{2}\sigma_z$ and the "fluxoid momentum" $f_z = \frac{1}{2}n\tau_z$ (given in terms of the fluxoid number n), all of them projected along the z direction. For a hybrid wire with

cylindrical symmetry, J_z commutes with H , $[J_z, H] = 0$, so that the eigenvalues $m_J = m_l + m_s + m_n$ of J_z are good quantum numbers of the eigenstates of H . Since $m_l \in \mathbb{Z}$ and $m_s \in \pm 1/2$, the possible eigenvalues m_J are [13]

$$m_J = \begin{cases} \mathbb{Z} + \frac{1}{2} & \text{if } n \text{ is even} \\ \mathbb{Z} & \text{if } n \text{ is odd} \end{cases}. \quad (\text{A2})$$

We can thus apply a canonical transformation $\mathcal{U} = e^{-i(m_J - \frac{1}{2}\sigma_z - \frac{1}{2}n\tau_z)\varphi}$ to reduce H to a φ -independent 4×4 effective Hamiltonian $\tilde{H} = \mathcal{U}H\mathcal{U}^\dagger$, where

$$\begin{aligned} \tilde{H} = & \left[\frac{p_z^2 + p_r^2}{2m} + U(r) - \mu \right] \sigma_0 \tau_z + V_Z \sigma_z \tau_0 \\ & + \frac{1}{2mr^2} \left(m_J - \frac{1}{2}\sigma_z - \frac{1}{2}n\tau_z + \frac{1}{2} \frac{\Phi}{\Phi_0} \frac{r^2}{R_{\text{LP}}^2} \tau_z \right)^2 \sigma_0 \tau_z \\ & - \frac{\alpha(r)}{r} \left(m_J - \frac{1}{2}\sigma_z - \frac{1}{2}n\tau_z + \frac{1}{2} \frac{\Phi}{\Phi_0} \frac{r^2}{R_{\text{LP}}^2} \tau_z \right) \sigma_z \tau_z \\ & + \alpha(r) k_z \sigma_y \tau_z + \Sigma_{\text{shell}}(\omega). \end{aligned} \quad (\text{A3})$$

Apart from the generalized angular momentum quantum number m_J , this Hamiltonian is expressed in terms of the longitudinal momentum operator $p_z = -i\partial_z$, the radial momentum operator $p_r = -i\partial_r$, $p_r^2 = -\frac{1}{r}\partial_r(r\partial_r)$, the semiconductor effective mass m , the chemical potential μ , the flux Φ and the superconducting flux quantum $\Phi_0 = h/2e$.

Even though it is not necessary for the appearance of the topological phase, we also consider the Zeeman effect produced by the magnetic field,

$$V_Z = \frac{1}{2}g\mu_B B_z, \quad (\text{A4})$$

where μ_B is the Bohr magneton and g is the semiconductor Landé g -factor.

$U(r)$ is the electrostatic potential energy inside the core. This potential is a consequence of the band-bending imposed by the epitaxial core/shell Ohmic contact, which in turn stems from the difference of the Al work function and the InAs electron affinity [50, 64]. We note that the degree of band-bending and precise shape of $U(r)$ depends on the microscopic details of the interface and the self-consistent electrostatic screening. We consider a simple model for $U(r)$ of the form

$$U(r) = U_{\text{min}} + (U_{\text{max}} - U_{\text{min}}) \left(\frac{r}{R} \right)^2, \quad (\text{A5})$$

for the solid-core nanowire, see Fig. 1(b).

Concerning the SOC inside the core, we assume it is of the Rashba type and produced by the inversion symmetry-breaking created the core/shell interface. It is thus radial and pointing outwards. For the solid-core nanowire and using a standard approximation from the 8-band model [65], we can write (see also [66])

$$\begin{aligned} \alpha(r) &= -\alpha_0 \partial_r U(r), \\ \alpha_0 &= \frac{P^2}{3} \left[\frac{1}{\Delta_g^2} - \frac{1}{(\Delta_{\text{soff}} + \Delta_g)^2} \right]. \end{aligned} \quad (\text{A6})$$

Taking the Kane parameter $P = 919.7$ meV nm, the semiconductor gap $\Delta_g = 417$ meV and split-off gap $\Delta_{\text{soff}} = 390$ meV, relevant for InAs, one obtains $\alpha_0 = 1.19$ nm². In our simulations, we take α_0 as a free parameter.

The form of the self energy for a diffusive shell in Eq. (A3), expressed in terms of a decay rate Γ_S from the core into the shell (in the normal state), has the expression [67]

$$\Sigma_{\text{shell}}(\omega) = \Gamma_S \sigma_0 \frac{\tau_x - u(\omega)\tau_0}{\sqrt{1 - u(\omega)^2}}. \quad (\text{A7})$$

Here, the complex function $u(\omega)$ is obtained from the equation

$$u(\omega) = \frac{\omega}{\Delta(\Lambda)} + \frac{\Lambda}{\Delta(\Lambda)} \frac{u(\omega)}{\sqrt{1 - u(\omega)^2}}, \quad (\text{A8})$$

where Λ is a pair breaking parameter (introduced by the magnetic field in our case) and the superconductor pairing amplitude Δ furthermore obeys

$$\begin{aligned} \ln \frac{\Delta(\Lambda)}{\Delta(0)} &= -P \left(\frac{\Lambda}{\Delta(\Lambda)} \right), \\ P(\lambda \leq 1) &= \frac{\pi}{4} \lambda, \\ P(\lambda \geq 1) &= \ln \left(\lambda + \sqrt{\lambda^2 - 1} \right) + \frac{\lambda}{2} \arctan \frac{1}{\sqrt{\lambda^2 - 1}} \\ &\quad - \frac{\sqrt{\lambda^2 - 1}}{2\lambda}, \end{aligned} \quad (\text{A9})$$

where $\Delta(0) \equiv \Delta_0$ is the pairing of a ballistic superconductor, i.e., for $\Lambda = 0$. Note that Λ has energy units and is bounded by $0 \leq \Lambda \leq \Delta_0/2$. The equation for $\Delta(\Lambda)$ has to be solved self-consistently. Equation (A8) can be rewritten as a fourth-order polynomial with root $u(\omega)$. We choose the solution that leads to the adequate continuity and asymptotic behavior of the retarded Green's functions. As a consequence, $u(\omega \rightarrow 0) \rightarrow 0$.

The superconductor energy gap is given by [67]

$$\Omega(\Lambda) = \left(\Delta(\Lambda)^{2/3} - \Lambda^{2/3} \right)^{3/2}. \quad (\text{A10})$$

It closes at $\Lambda = e^{-\pi/4} \Delta_0$, while the pairing becomes zero at $\Lambda = \Delta_0/2$, yielding a gapless superconductor region between these two values of the depairing. Notice that for such region our model is still valid, but for $\Lambda > \Delta_0/2$, Δ vanishes and the material becomes a metal, with the normal self-energy

$$\Sigma_{\text{shell}}^{\Lambda > \Delta_0/2}(\omega) = -i\Gamma_S \sigma_0 \tau_0. \quad (\text{A11})$$

Assuming cylindrical symmetry, a standard Ginzburg-Landau theory of the LP effect [48, 68–71] provides an explicit connection between depairing and flux,

$$\begin{aligned} \Lambda(\Phi) &= \frac{k_B T_c \xi_d^2}{\pi R_{\text{LP}}^2} \left[4 \left(n - \frac{\Phi}{\Phi_0} \right)^2 + \frac{d^2}{R_{\text{LP}}^2} \left(\frac{\Phi^2}{\Phi_0^2} + \frac{n^2}{3} \right) \right], \\ n(\Phi) &= [\Phi/\Phi_0] = 0, \pm 1, \pm 2, \dots \end{aligned} \quad (\text{A12})$$

where ξ_d is the diffusive superconducting coherence length and T_c is the zero-flux critical temperature. At zero field $\Lambda(0) = 0$ and $k_B T_c \approx \Delta_0/1.76$, where k_B is the Boltzmann constant. The way in which $\Lambda(\Phi)$ depends on Φ gives rise to modulations of the shell gap with flux, defining different regions called LP lobes with fixed fluxoid n . The shell gap $\Omega(\Phi)$ is maximum at the center of the lobes, for $\Phi = n\Phi_0$, and it decreases towards the lobe edges. In the non-destructive LP regime the shell gap does not close in between lobes, at half-integer flux $\Phi = (n/2)\Phi_0$. This is the case analyzed in the main text. When the depairing at $\Phi = (n/2)\Phi_0$ is larger than $\Lambda = e^{-\pi/4} \Delta_0$, the shell transitions into the destructive LP regime; this is the case analyzed in Appendix C. The destructive LP regime, defined when a destructive region appears between the $n = 0$ and $n = 1$ lobes, occurs for

$$C \frac{R_{\text{LP}}^2}{\xi_d^2} - \frac{d^2}{4R_{\text{LP}}^2} \leq 1, \quad (\text{A13})$$

where $C = \pi e^{-\pi/4} \Delta_0 / k_B T_c \approx 2.52$. When $d \rightarrow 0$, the destructive regime happens for $R_{\text{LP}}/\xi_d \lesssim 0.6$ [48].

1. Tubular-core approximation

In the case of a tubular-core nanowire, when the semiconductor thickness W is small as compared to R , see Fig. 1(a), we can make some approximations to the Hamiltonian (A3). For the lowest radial momentum subband, $m_r = 0$, it is possible to concentrate all the wave function at an average radius R_{av} within the semiconductor tube section, see Ref. [36]. We can thus substitute $r = R_{\text{av}}$ in Eq. (A3). Defining $\tilde{\mu} \equiv \mu - U(R_{\text{av}}) - \langle p_r^2 \rangle / 2m$, where $\langle p_r^2 \rangle / 2m$ represents the radial confinement energy, we can write the tubular-core BdG effective Hamiltonian as

$$\begin{aligned} \tilde{H}^{TC} &= \left(\frac{p_z^2}{2m} - \tilde{\mu} \right) \sigma_0 \tau_z + V_Z \sigma_z \tau_0 \\ &+ \frac{1}{2m R_{\text{av}}^2} \left(m_J - \frac{1}{2} \sigma_z - \frac{1}{2} n \tau_z + \frac{1}{2} \frac{\Phi}{\Phi_0} \frac{R_{\text{av}}^2}{R_{\text{LP}}^2} \tau_z \right)^2 \sigma_0 \tau_z \\ &- \frac{\alpha}{R_{\text{av}}} \left(m_J - \frac{1}{2} \sigma_z - \frac{1}{2} n \tau_z + \frac{1}{2} \frac{\Phi}{\Phi_0} \frac{R_{\text{av}}^2}{R_{\text{LP}}^2} \tau_z \right) \sigma_z \tau_z \\ &+ \alpha k_z \sigma_y \tau_z + \Sigma_{\text{shell}}(\omega). \end{aligned} \quad (\text{A14})$$

Note that $\tilde{\mu}$ represents now the Fermi energy (or energy difference between the highest and lowest occupied single-particle states at zero temperature). Moreover, the SOC can be approximated by a constant α . The form of the self energy term remains unchanged, but it is now understood to act at $r = R_{\text{av}}$ (instead of at $r = R$ like in the solid-core model). This was dubbed the modified hollow-core approximation of the Hamiltonian in Ref. [36].

It is possible [13] to rewrite Eq. (A14) as

$$\tilde{H}^{\text{TC}} = \left(\frac{p_z^2}{2m} - \tilde{\mu}_{m_J}^\phi \right) \sigma_0 \tau_z + (V_Z + V_Z^\phi) \sigma_z + A_{m_J} + C_{m_J} \sigma_z \tau_z + \alpha k_z \sigma_y \tau_z + \Sigma_{\text{shell}}(\omega), \quad (\text{A15})$$

where

$$\tilde{\mu}_{m_J}^\phi = \tilde{\mu} - \frac{\alpha}{2R_{\text{av}}} - \frac{1}{8mR_{\text{av}}^2} (4m_J^2 + 1 + \phi^2) \quad (\text{A16})$$

$$V_Z^\phi = \frac{1}{2} \phi \left(\frac{1}{2mR_{\text{av}}^2} + \frac{\alpha}{R_{\text{av}}} \right), \quad (\text{A17})$$

$$A_{m_J} = -m_J \frac{1}{2mR_{\text{av}}^2} \phi, \quad (\text{A18})$$

$$C_{m_J} = -m_J \left(\frac{1}{2mR_{\text{av}}^2} + \frac{\alpha}{R_{\text{av}}} \right), \quad (\text{A19})$$

with $\phi = n - \Phi(R_{\text{av}})/\Phi_0$. For $m_J = 0$, $A_{m_J} = C_{m_J} = 0$ and it is then possible to map this Hamiltonian to the conventional single-band Oreg-Lutchyn nanowire model [9, 10]. Note that the *effective* Zeeman term V_Z^ϕ has an orbital origin here, and it is present even in the absence of semiconductor g factor. Thanks to this mapping, it is possible to understand that when the wire is threaded by an odd number of fluxoids n , the $m_J = 0$ subband sector may undergo a topological phase transition and develop MBSs (if the parameters of the wire are such that the topological phase falls within the corresponding lobe).

Appendix B: Period of Majorana oscillations

In a Majorana nanowire of length L in the topological phase, the wavefunction of the MBSs at the ends of the wire are exponentially localized around each end as $\sim e^{-|z-z_{\text{end}}|/\xi_M}$, where ξ_M is the Majorana localization length. In Ref. [21] it was shown that the exponential decay, however, is also spatially modulated, oscillating as $\sim \cos(k_F z)$, where k_F is the (outer) Fermi wavevector. As a result, two overlapping Majoranas localized at opposite ends will hybridize across the length- L nanowire with a typical splitting of the form $\sim e^{-2L/\xi_M} \cos(k_F L)$. The dependence of k_F with wire parameters, such as e.g. the chemical potential μ , the Zeeman splitting V_Z or, in full-shell wires, the flux Φ , leads to oscillations of the Majorana splitting as a function of said parameters.

The instantaneous period δx of the Majorana oscillations as a function of any parameter x is given by

$$\delta x = \left| \frac{2\pi}{L \partial_x k_F(x)} \right|. \quad (\text{B1})$$

This expression results from linearizing $k_F(x + \delta x)L \approx k_F(x)L + \delta x \partial_x k_F(x)L$, and equating the last term to a full 2π phase shift of the cosine. The above applies equally to an Oreg-Lutchyn nanowire as to a full-shell nanowire. Here we are interested in the latter, where in particular the tuning parameter x is the flux Φ . We will derive

the Majorana flux period $\delta\Phi$ in the particular case of the tubular-core model, for which we have the simple analytical mapping to the Oreg-Lutchyn model explained in Appendix A 1, and can thus derive a simple form for $k_F(\Phi)$.

We proceed as follows. We first diagonalize the tubular-core Hamiltonian (A15) but in the absence of the superconductor and for $m_J = 0$, i.e., the normal single-band semiconductor Hamiltonian

$$\tilde{H}_0^{\text{TC}}(k_z) = \frac{k_z^2}{2m} - \tilde{\mu}^\phi + \alpha k_z \sigma_y + (V_Z + V_Z^\phi) \sigma_z, \quad (\text{B2})$$

where k_z is the longitudinal wave vector and

$$\tilde{\mu}^\phi = \tilde{\mu} - \frac{\alpha}{2R_{\text{av}}} - \frac{1}{8mR_{\text{av}}^2} (1 + \phi^2) \quad (\text{B3})$$

is the same as Eq. (A16) but for $m_J = 0$. We then equate the eigenvalues to zero to find solutions for $k_z = k_F$. These come in two types: two solutions with high $|k_z|$ (called ‘‘outer’’ solution), another two with small $|k_z|$ (‘‘inner’’), that actually become zero at the helical transition $|V_Z^\phi| = |\tilde{\mu}^\phi|$. The Majorana oscillations are controlled by the outer solution, which takes the explicit form

$$k_F = \sqrt{2m} \sqrt{m\alpha^2 + \tilde{\mu}^\phi + \epsilon_\phi}, \quad (\text{B4})$$

$$\epsilon_\phi = \sqrt{(V_Z + V_Z^\phi)^2 + m^2\alpha^4 + 2m\alpha^2\tilde{\mu}^\phi}.$$

Some authors have formulated alternative expressions for k_F (in the Zeeman-driven Oreg-Lutchyn model) that remain accurate also for finite Δ at the expense of making $\alpha = 0$, and viceversa [21].

Inserting Eqs. (A17) and (B3) into Eqs. (B4) and applying Eq. (B1) with $x = \Phi$ yields the Majorana oscillation period with flux in the odd- n LP lobe

$$\frac{\delta\Phi}{\Phi_0} = \quad (\text{B5})$$

$$\frac{8\pi\epsilon_\phi k_F R_{\text{LP}}^2/L}{(\epsilon_\phi + m\alpha^2) \left[n - (n - \frac{1}{2}) \frac{R_{\text{av}}^2}{R_{\text{LP}}^2} \right] - (V_Z + V_Z^\phi)(1 + 2mR_{\text{av}}\alpha)}.$$

To assess whether at least one Majorana oscillation is visible within an odd lobe, one must compare $\delta\Phi$ to the flux interval $I_\Phi^n = \Phi_R - \Phi_L$ that contains MBSs for lobe n . Here Φ_L and Φ_R are the minimum and maximum flux with MBSs in the lobe, respectively. A Majorana oscillation will then be visible within the lobe only if $\delta\Phi < I_\Phi^n$. Assuming a Majorana mode is indeed present within the n lobe, and approximating the shell thickness by $d \approx 0$, Eq. (A10) yields a simple form for Φ_L (i.e. the left side of lobe n), $\Phi_L \approx \Phi_0 \max[n - \frac{1}{2}, n - 1.74R_{\text{LP}}/\xi_d]$. Φ_R , the highest flux in the lobe with a Majorana mode, similarly reduces to $\Phi_R = \Phi_0 \min[n + \frac{1}{2}, n + 1.74R_{\text{LP}}/\xi_d, \Phi_c/\Phi_0]$. Here Φ_c is the critical flux, namely the Φ solution of the equation $\Delta^2 + (\tilde{\mu}^\phi)^2 - (V_Z^\phi)^2 = 0$.

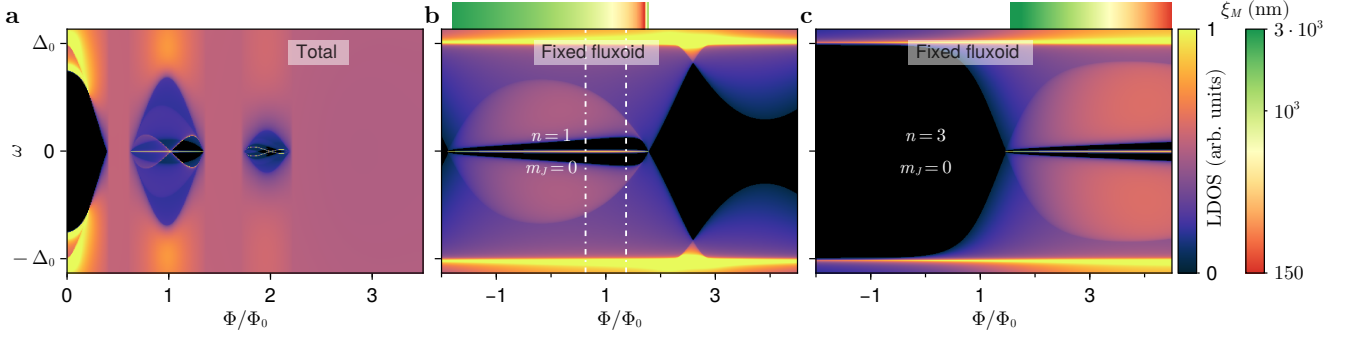


FIG. 6. **Tubular-core nanowire of semi-infinite length in the destructive Little-Parks regime.** Same as Fig. 2 but for a tubular-core nanowire with $d = 10$ nm, $R = 30$ nm and $W = 10$ nm. The wire is in the destructive LP regime, so that there are gapless regions between lobes and the $n = 3$ lobe is closed. Other parameters: $\alpha = 10$ meVnm, $\mu = 39.1$ meV, $g = 10$, $\Gamma_S = 8\Delta_0$, $\Delta_0 = 0.23$ meV, $\xi_d = 70$ nm. Minimum ξ_M inside lobe $n = 1$: ~ 450 nm.

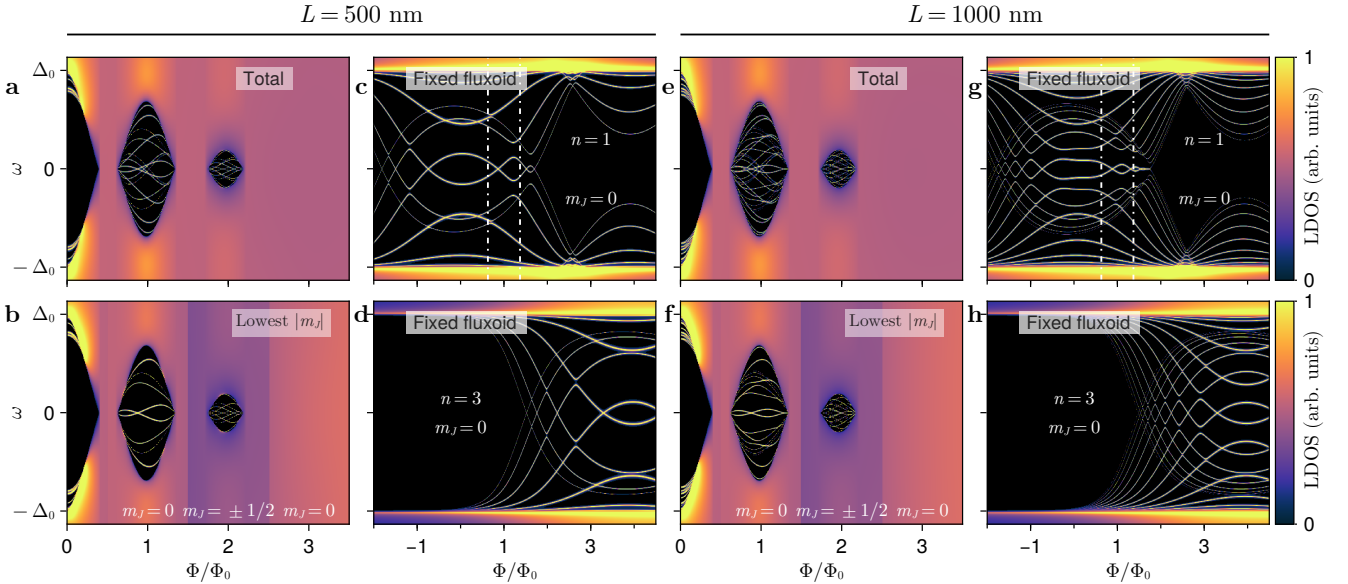


FIG. 7. **Tubular-core nanowire of finite length in the destructive Little-Parks regime.** Same as Fig. 3 but for a tubular-core nanowire with $d = 10$ nm, $R = 30$ nm and $W = 10$ nm. Other parameters like in Fig. 6.

The condition for full oscillations, $\delta\Phi < I_{\Phi}^n$, is never satisfied in lobes $n = 1$ and $n = 3$ for the typical range of parameters of InAs full-shell nanowires ($m = 0.023m_e$, $\xi_d \in [40, 250]$ nm, $L < 1.5$ μ m, $R_{LP} \geq R_{av} > 40$ nm, $\alpha > 5$ meVnm and $\Delta > 0.05$ meV). The choice of parameters that maximizes the probability of satisfying the condition and hence of fitting at least one oscillation within the lobe corresponds to long ($L > 2\mu$ m) and narrow ($R_{LP} < 40$ nm) nanowires. The constraint on R_{LP} is slightly relaxed for higher lobes $n \geq 5$ if $\alpha \lesssim 20$ meVnm, so that oscillations in $R_{LP} < 50$ nm wires becomes possible, as long as these higher lobes remain open and measurable. This parameter window, however, is quite narrow.

Appendix C: Destructive Little-Parks regime

In the main text we have considered a representative case of an Al/InAs full-shell hybrid nanowire in the non-destructive LP regime ($d = 10$ nm, $R = 70$ nm and $\xi_d = 70$ nm). In this Appendix we analyze a representative case in the destructive LP regime, a narrower full-shell hybrid nanowire (with $R = 30$ nm but with the same shell thickness $d = 10$ nm and coherence length $\xi_d = 70$ nm).

1. Tubular-core model

We first consider the tubular-core model for the full-shell nanowire, with a semiconductor tube thickness $W =$

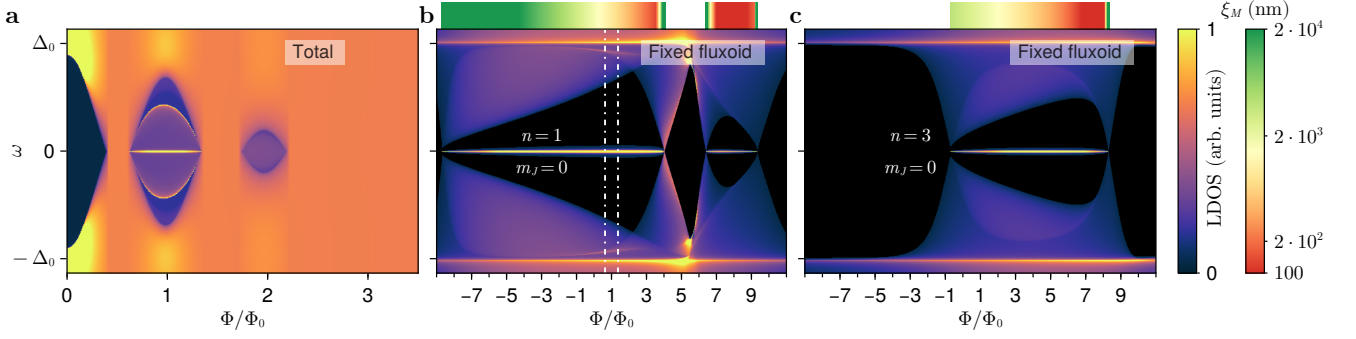


FIG. 8. **Solid-core nanowire of semi-infinite length in the destructive Little-Parks regime.** Same as Fig. 2 but for a solid-core nanowire with $d = 10$ nm and $R = 30$ nm. The radial dome-like electrostatic potential profile inside the semiconductor has $U_{\min} = -30$ meV and $U_{\max} = 0$, with $\mu = 2$ meV. Other parameters like in Fig. 6, except for $\langle \alpha \rangle = 8.6$ meVnm and $\Gamma_S = 40\Delta_0$. Minimum ξ_M inside lobe $n = 1$: ~ 210 nm.

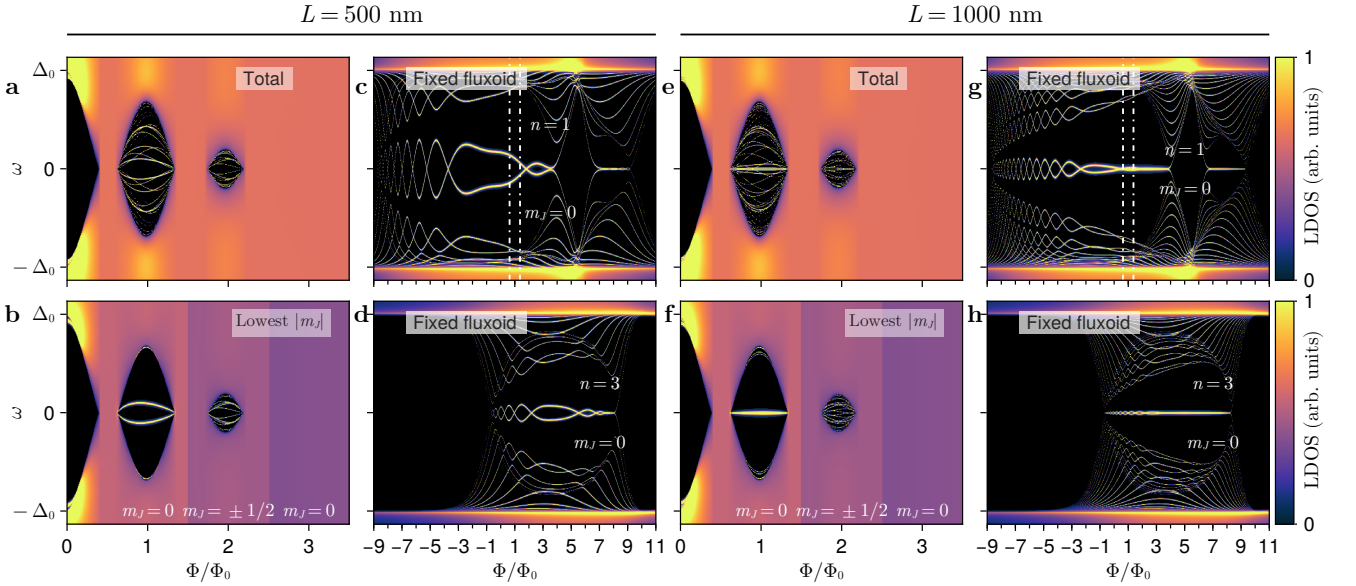


FIG. 9. **Solid-core nanowire of finite length in the destructive Little-Parks regime.** Same as Fig. 3 but for a solid-core nanowire with $d = 10$ nm and $R = 30$ nm. Other parameters like in Fig. 8.

10 nm. In analogy to Fig. 2 of the main text, in Fig. 6(a) we plot the LDOS at the end of a semi-infinite nanowire as a function of normalized flux. Since the wire is in the destructive LP regime, now there are gapless regions between LP lobes for fluxes around half-integer multiples of the superconducting flux quantum Φ_0 . Note that the maximum lobe height decreases with the lobe number n (as corresponds to a wire with finite d), as well as the lobe flux window. For these parameters, the $n = 3$ lobe (and subsequent ones) is already closed. The wire is in the topological regime and a Majorana ZEP can be seen crossing the whole $n = 1$ lobe. Additionally, low lying CdGM analog states disperse with flux and cross zero energy in both the $n = 1, 2$ lobes. A topological minigap at the right end of the first LP lobe can be observed.

The $m_J = 0$, $n = 1$ fixed-fluxoid simulation analogous to Fig. 2(b), is presented in Fig. 6(b). We can observe that the Majorana localization length ξ_M (depicted above the panel) is dominated by the outer ($k_z = k_F$) $m_J = 0$ gap. (A similar simulation for $n = 3$ is presented in Fig. 6(c), although in this case it is irrelevant since the third lobe is closed).

The case of a finite-length tubular-core hybrid nanowire is analyzed in Fig. 7. For $L = 500$ nm, the $m_J = 0$ contribution to the LDOS in the first lobe, Fig. 7(b), shows what appears to be a couple of Majorana oscillations versus flux. By checking the $n = 1$ fixed-fluxoid plot of Fig. 7(c), we can understand that it is just a single Majorana parity crossing. The split levels go to zero energy at the lobe edges in Fig. 7(b) as a consequence of

the LP parent gap closing. Thus, in this case there are no complete Majorana oscillations within the lobe either. Incidentally, we note that in Fig. 7(b) there are color discontinuities at half integer Φ/Φ_0 values. These are non physical, just artifacts of selecting the lowest $|m_J|$ contribution to the total LDOS. The complete sum, Fig. 7(a), is continuous (although not its first derivative with respect to flux). A similar study for $L = 1000$ nm is shown on the right half of Fig. 7. Although one could interpret that there are a couple of oscillations in the first lobe of Fig. 7(f), in this case there is only one true complete Majorana oscillation according to Fig. 7(g).

The possible presence of Majorana oscillations in the first lobe of Figs. 7(a,e) is accompanied, and thus masked, by the presence of zero-energy crossings and apparent oscillations of other subgap levels. Again, these apparent oscillations come from a combination of the dispersion with flux of the CdGM levels and the parent-gap closing at the lobe edges. In principle, one could distinguish between Majoranas and CdGM states in dI/dV measurements because the Majorana levels are states bound to the hybrid wire end, thus more strongly coupled to the tunnel-contact probe, whereas the CdGM states are delocalized along the length of the wire. This should translate into different total peak weight in tunneling spectroscopy. However, the Majorana localization length ξ_M and the nanowire length L in realistic experiments are often not that different, so the peak weight difference may be small.

We emphasize that the hybrid wire analyzed in this section is a borderline case where the Majorana oscillation period is comparable to or slightly smaller than the flux interval that contains Majoranas for the $n = 1$ lobe, $\delta\Phi \sim I_{\Phi}^{n=1}$. In general, for other (realistic) parameters, we find $\delta\Phi \gtrsim I_{\Phi}^n$ as discussed in the main text and Ap-

pendix B.

2. Solid-core model

Finally, we consider a solid-core full-shell hybrid nanowire in the destructive LP regime. The case of a semi-infinite wire can be seen in Fig. 8. As in the tubular-core case of Fig. 6(a), there are gapless flux intervals between lobes and the third and subsequent LP lobes have disappeared altogether. A Majorana ZEP is also present across the whole $n = 1$ lobe, but now there is no topological minigap at any flux. As in the solid-core case of Fig. 4 in the main text, the Majorana zero mode coexists with a LDOS background coming from the rest of the occupied CdGM analogs. This is the typical behaviour of solid-core full-shell nanowires. The Majorana localization length is $\xi_M \approx 210$ nm for the parameters selected in this figure.

For a $L = 500$ nm hybrid nanowire we find that the Majorana modes split in energy, as corresponds to overlapping left- and right-end MBSs, see Fig. 9(b), but there is not a single Majorana oscillation inside the lobe, as can be checked in Fig. 9(c). The closing of the split peaks at the lobe edges in Fig. 9(b) is a consequence of the parent-gap closing at the lobe edges in the destructive LP regime. In this case, the CdGM levels do not cross zero energy and are in general at higher energies than the Majorana states, as can be seen in Fig. 9(a). For a longer hybrid nanowire, there could be in principle more chances to observe Majorana oscillations within the first lobe. However, this is not the case, see Fig. 9(e). The Majorana splitting is so small, see Fig. 9(f), that it could be mistaken with a true Majorana zero mode. In this case, only the longitudinally-confined CdGM levels reveal that the wire has indeed a finite length.

-
- [1] A. Yu. Kitaev, Fault-tolerant quantum computation by anyons, *Annals of Physics* **303**, 2 (2003).
- [2] S. D. Sarma, M. Freedman, and C. Nayak, Majorana zero modes and topological quantum computation, *npj Quantum Inf* **1**, 1 (2015).
- [3] C. Nayak, S. H. Simon, A. Stern, M. Freedman, and S. Das Sarma, Non-Abelian anyons and topological quantum computation, *Rev. Mod. Phys.* **80**, 1083 (2008).
- [4] R. Aguado and L. P. Kouwenhoven, Majorana qubits for topological quantum computing, *Physics Today* **73**, 44 (2020).
- [5] A. Yazdani, F. von Oppen, B. I. Halperin, and A. Yacoby, Hunting for Majoranas, *Science* **380**, eade0850 (2023).
- [6] J. Alicea, New directions in the pursuit of Majorana fermions in solid state systems, *Rep. Prog. Phys.* **75**, 076501 (2012).
- [7] C. Beenakker, Search for non-Abelian Majorana braiding statistics in superconductors, *SciPost Physics Lecture Notes*, 015 (2020).
- [8] R. Aguado, Majorana quasiparticles in condensed matter, *Riv. Nuovo Cim.* **40**, 523 (2017).
- [9] R. M. Lutchyn, J. D. Sau, and S. Das Sarma, Majorana Fermions and a Topological Phase Transition in Semiconductor-Superconductor Heterostructures, *Phys. Rev. Lett.* **105**, 077001 (2010).
- [10] Y. Oreg, G. Refael, and F. von Oppen, Helical Liquids and Majorana Bound States in Quantum Wires, *Phys. Rev. Lett.* **105**, 177002 (2010).
- [11] V. Mourik, K. Zuo, S. M. Frolov, S. R. Plissard, E. P. A. M. Bakkers, and L. P. Kouwenhoven, Signatures of Majorana Fermions in Hybrid Superconductor-Semiconductor Nanowire Devices, *Science* **336**, 1003 (2012).
- [12] S. Vaitiekėnas, Y. Liu, P. Krogstrup, and C. M. Marcus, Zero-bias peaks at zero magnetic field in ferromagnetic hybrid nanowires, *Nat. Phys.* **17**, 43 (2021).
- [13] S. Vaitiekėnas, G. W. Winkler, B. van Heck, T. Karzig, M.-T. Deng, K. Flensberg, L. I. Glazman, C. Nayak, P. Krogstrup, R. M. Lutchyn, and C. M. Marcus, Flux-induced topological superconductivity in full-shell

- nanowires, *Science* **367**, eaav3392 (2020).
- [14] M. Valentini, M. Borovkov, E. Prada, S. Martí-Sánchez, M. Botifoll, A. Hofmann, J. Arbiol, R. Aguado, P. San-Jose, and G. Katsaros, Majorana-like Coulomb spectroscopy in the absence of zero-bias peaks, *Nature* **612**, 442 (2022).
- [15] M.-T. Deng, S. Vaitiekėnas, E. Prada, P. San-Jose, J. Nygård, P. Krogstrup, R. Aguado, and C. M. Marcus, Nonlocality of Majorana modes in hybrid nanowires, *Phys. Rev. B* **98**, 085125 (2018).
- [16] Microsoft Quantum, InAs-Al hybrid devices passing the topological gap protocol, *Phys. Rev. B* **107**, 245423 (2023).
- [17] Microsoft Quantum, Interferometric Single-Shot Parity Measurement in an InAs-Al Hybrid Device (2024), arXiv:2401.09549 [cond-mat].
- [18] E. Prada, P. San-Jose, M. W. A. de Moor, A. Geresdi, E. J. H. Lee, J. Klinovaja, D. Loss, J. Nygård, R. Aguado, and L. P. Kouwenhoven, From Andreev to Majorana bound states in hybrid superconductor–semiconductor nanowires, *Nat Rev Phys* **2**, 575 (2020).
- [19] E. Prada, P. San-Jose, and R. Aguado, Transport spectroscopy of SNS nanowire junctions with Majorana fermions, *Phys. Rev. B* **86**, 180503 (2012).
- [20] C.-X. Liu, J. D. Sau, T. D. Stanescu, and S. Das Sarma, Andreev bound states versus Majorana bound states in quantum dot–nanowire–superconductor hybrid structures: Trivial versus topological zero-bias conductance peaks, *Phys. Rev. B* **96**, 075161 (2017).
- [21] S. Das Sarma, J. D. Sau, and T. D. Stanescu, Splitting of the zero-bias conductance peak as smoking gun evidence for the existence of the Majorana mode in a superconductor–semiconductor nanowire, *Phys. Rev. B* **86**, 220506 (2012).
- [22] J. Klinovaja and D. Loss, Composite Majorana fermion wave functions in nanowires, *Phys. Rev. B* **86**, 085408 (2012).
- [23] J. S. Lim, L. ç Serra, R. López, and R. Aguado, Magnetic-field instability of Majorana modes in multiband semiconductor wires, *Phys. Rev. B* **86**, 121103 (2012).
- [24] C. Fleckenstein, F. Domínguez, N. Traverso Ziani, and B. Trauzettel, Decaying spectral oscillations in a Majorana wire with finite coherence length, *Phys. Rev. B* **97**, 155425 (2018).
- [25] Z. Cao, H. Zhang, H.-F. Lü, W.-X. He, H.-Z. Lu, and X. C. Xie, Decays of majorana or andreev oscillations induced by steplike spin-orbit coupling, *Physical Review Letters* **122** (2019).
- [26] J. Cayao, P. San-Jose, A. M. Black-Schaffer, R. Aguado, and E. Prada, Majorana splitting from critical currents in Josephson junctions, *Phys. Rev. B* **96**, 205425 (2017).
- [27] W. A. Little and R. D. Parks, Observation of Quantum Periodicity in the Transition Temperature of a Superconducting Cylinder, *Phys. Rev. Lett.* **9**, 9 (1962).
- [28] R. D. Parks and W. A. Little, Fluxoid Quantization in a Multiply-Connected Superconductor, *Phys. Rev.* **133**, A97 (1964).
- [29] M. Tinkham, *Introduction to Superconductivity*, 2nd ed., International Series in Pure and Applied Physics (McGraw Hill, 1996).
- [30] C. Caroli, P. G. De Gennes, and J. Matricon, Bound Fermion states on a vortex line in a type II superconductor, *Physics Letters* **9**, 307 (1964).
- [31] E. Brun Hansen, The bound excitations of a single vortex in a pure type II superconductor, *Physics Letters A* **27**, 576 (1968).
- [32] A. A. Kopasov and A. S. Mel'nikov, Influence of the Accumulation Layer on the Spectral Properties of Full-Shell Majorana Nanowires, *Phys. Solid State* **62**, 1592 (2020).
- [33] A. A. Kopasov and A. S. Mel'nikov, Multiple topological transitions driven by the interplay of normal scattering and Andreev scattering, *Phys. Rev. B* **101**, 054515 (2020).
- [34] P. San-Jose, C. Payá, C. M. Marcus, S. Vaitiekėnas, and E. Prada, Theory of Caroli–de Gennes–Matricon analogs in full-shell hybrid nanowires, *Phys. Rev. B* **107**, 155423 (2023).
- [35] F. Peñaranda, R. Aguado, P. San-Jose, and E. Prada, Even-odd effect and Majorana states in full-shell nanowires, *Phys. Rev. Res.* **2**, 023171 (2020).
- [36] C. Payá, S. D. Escribano, A. Vezzosi, F. Peñaranda, R. Aguado, P. San-Jose, and E. Prada, Phenomenology of Majorana zero modes in full-shell hybrid nanowires, *Phys. Rev. B* **109**, 115428 (2024).
- [37] B. D. Woods, S. Das Sarma, and T. D. Stanescu, Electronic structure of full-shell InAs/Al hybrid semiconductor–superconductor nanowires: Spin-orbit coupling and topological phase space, *Phys. Rev. B* **99**, 161118 (2019).
- [38] S. Vaitiekėnas, P. Krogstrup, and C. M. Marcus, Anomalous metallic phase in tunable destructive superconductors, *Phys. Rev. B* **101**, 060507 (2020).
- [39] M. Valentini, F. Peñaranda, A. Hofmann, M. Brauns, R. Hauschild, P. Krogstrup, P. San-Jose, E. Prada, R. Aguado, and G. Katsaros, Nontopological zero-bias peaks in full-shell nanowires induced by flux-tunable Andreev states, *Science* **373**, 82 (2021).
- [40] A. Vekris, J. C. Estrada Saldaña, J. de Bruijckere, S. Lorić, T. Kanne, M. Marnauza, D. Olsteins, J. Nygård, and K. Grove-Rasmussen, Asymmetric Little–Parks oscillations in full shell double nanowires, *Sci Rep* **11**, 19034 (2021).
- [41] S. D. Escribano, A. Levy Yeyati, R. Aguado, E. Prada, and P. San-Jose, Fluxoid-induced pairing suppression and near-zero modes in quantum dots coupled to full-shell nanowires, *Phys. Rev. B* **105**, 045418 (2022).
- [42] D. Razmadze, R. S. Souto, E. C. T. O'Farrell, P. Krogstrup, M. Leijnse, C. M. Marcus, and S. Vaitiekėnas, Supercurrent transport through 1e-periodic full-shell Coulomb islands, *Phys. Rev. B* **109**, L041302 (2024).
- [43] G. Giavaras and R. Aguado, Flux-tunable supercurrent in full-shell nanowire Josephson junctions, *Phys. Rev. B* **109**, 024509 (2024).
- [44] K. O. Klausen, A. Sitek, S. I. Erlingsson, and A. Manolescu, Flux-periodic oscillations in proximitized core–shell nanowires, *Nanotechnology* **34**, 345001 (2023).
- [45] A. Ibabe, M. Gómez, G. O. Steffensen, T. Kanne, J. Nygård, A. L. Yeyati, and E. J. H. Lee, Joule spectroscopy of hybrid superconductor–semiconductor nanodevices, *Nat Commun* **14**, 2873 (2023).
- [46] Á. Ibabe, G. O. Steffensen, I. Casal, M. Gómez, T. Kanne, J. Nygård, A. Levy Yeyati, and E. J. H. Lee, Heat Dissipation Mechanisms in Hybrid Superconductor–Semiconductor Devices Revealed by Joule Spectroscopy, *Nano Lett.* **24**, 6488 (2024).
- [47] A. Vezzosi, C. Payá, P. Wójcik, A. Bertoni, G. Goldoni,

- E. Prada, and S. D. Escribano, InP/GaSb core-shell nanowires: A practical proposal for Majorana modes in a full-shell hybrid geometry with hole bands (2024), arXiv:2405.07651 [cond-mat].
- [48] G. Schwiete and Y. Oreg, Fluctuation persistent current in small superconducting rings, *Phys. Rev. B* **82**, 214514 (2010).
- [49] A. E. Antipov, A. Bargerbos, G. W. Winkler, B. Bauer, E. Rossi, and R. M. Lutchyn, Effects of Gate-Induced Electric Fields on Semiconductor Majorana Nanowires, *Phys. Rev. X* **8**, 031041 (2018).
- [50] A. E. G. Mikkelsen, P. Kotetes, P. Krogstrup, and K. Flensberg, Hybridization at Superconductor-Semiconductor Interfaces, *Phys. Rev. X* **8**, 031040 (2018).
- [51] H. Pan and S. Das Sarma, Physical mechanisms for zero-bias conductance peaks in Majorana nanowires, *Phys. Rev. Res.* **2**, 013377 (2020).
- [52] S. Das Sarma and H. Pan, Disorder-induced zero-bias peaks in Majorana nanowires, *Phys. Rev. B* **103**, 195158 (2021).
- [53] S. Das Sarma, In search of Majorana, *Nat. Phys.* **19**, 165 (2023).
- [54] G. Kells, D. Meidan, and P. W. Brouwer, Near-zero-energy end states in topologically trivial spin-orbit coupled superconducting nanowires with a smooth confinement, *Phys. Rev. B* **86**, 100503 (2012).
- [55] D. Rainis, L. Trifunovic, J. Klinovaja, and D. Loss, Towards a realistic transport modeling in a superconducting nanowire with Majorana fermions, *Phys. Rev. B* **87**, 024515 (2013).
- [56] D. Roy, N. Bondyopadhyaya, and S. Tewari, Topologically trivial zero-bias conductance peak in semiconductor Majorana wires from boundary effects, *Phys. Rev. B* **88**, 020502 (2013).
- [57] F. Peñaranda, R. Aguado, P. San-Jose, and E. Prada, Quantifying wave-function overlaps in inhomogeneous Majorana nanowires, *Phys. Rev. B* **98**, 235406 (2018).
- [58] A. Vuik, B. Nijholt, A. R. Akhmerov, and M. Wimmer, Reproducing topological properties with quasi-Majorana states, *SciPost Physics* **7**, 061 (2019).
- [59] C. Payá *et al.* (in preparation).
- [60] P. San-Jose, Pablosanjose/Quantica.jl: V1.1.0, Zenodo (2024).
- [61] C. Payá, CarlosP24/SP38.Finite.Length: 24.07 ArXiv, Zenodo (2024).
- [62] C. Payá, CarlosP24/FullShell.jl: Full-shell semi-infinite nanowire Hamiltonian builder - destructive LP improved, Zenodo (2024).
- [63] S. Danisch and J. Krumbiegel, Makie.jl: Flexible high-performance data visualization for Julia, *J. Open Source Softw.* **6**, 3349 (2021).
- [64] C.-X. Liu, S. Schuwalow, Y. Liu, K. Vilkelis, A. L. R. Manesco, P. Krogstrup, and M. Wimmer, Electronic properties of InAs/EuS/Al hybrid nanowires, *Phys. Rev. B* **104**, 014516 (2021).
- [65] R. Winkler, *Spin—Orbit Coupling Effects in Two-Dimensional Electron and Hole Systems*, Springer Tracts in Modern Physics, Vol. 191 (Springer, Berlin, Heidelberg, 2003).
- [66] S. D. Escribano, A. L. Yeyati, and E. Prada, Improved effective equation for the Rashba spin-orbit coupling in semiconductor nanowires, *Phys. Rev. Res.* **2**, 033264 (2020).
- [67] S. Skalski, O. Betbeder-Matibet, and P. R. Weiss, Properties of Superconducting Alloys Containing Paramagnetic Impurities, *Phys. Rev.* **136**, A1500 (1964).
- [68] A. V. Lopatin, N. Shah, and V. M. Vinokur, Fluctuation Conductivity of Thin Films and Nanowires Near a Parallel-Field-Tuned Superconducting Quantum Phase Transition, *Phys. Rev. Lett.* **94**, 037003 (2005).
- [69] N. Shah and A. Lopatin, Microscopic analysis of the superconducting quantum critical point: Finite-temperature crossovers in transport near a pair-breaking quantum phase transition, *Phys. Rev. B* **76**, 094511 (2007).
- [70] V. H. Dao and L. F. Chibotaru, Destruction of global coherence in long superconducting nanocylinders, *Phys. Rev. B* **79**, 134524 (2009).
- [71] I. Sternfeld, E. Levy, M. Eshkol, A. Tsukernik, M. Karpovskii, H. Shtrikman, A. Kretinin, and A. Palevski, Magnetoresistance Oscillations of Superconducting Al-Film Cylinders Covering InAs Nanowires below the Quantum Critical Point, *Phys. Rev. Lett.* **107**, 037001 (2011).